3.1 Introduction

It's been decades of discovery of a smart, efficient hybrid material known as MOF. According to literature, more than 70,000 MOFs are fabricated using various SBUs and organic linkers. It has attracted researchers because of its exotic properties like high thermal stability, porous crystalline structure, ultra-high specific surface area, low density etc [1]. It's a class of coordination polymer that has found versatile application in the fields ranging from drug delivery to gas storage. In order to avail this framework in the field of electronics or electrochemical assets as electrodes or membranes in energy storage applications like fuel cells, supercapacitors, sensors, batteries, solar cells etc., strategies should be applied to generate charge carriers as well as conduction pathways within the framework [2] . So far approaches have been made to introduce free charge carriers by designing redox active ligands, π- conjugated organic molecules, donor-acceptor pairs, redox active metal centres, mix-metal nodes etc. [3]. For instance, Jihye Park and his group reported a cobalt-based 2D conductive metal−organic framework (MOF) redox-active linker hexaaminobenzene (HAB), and a Co (II) as metal center with electrical conductivity as high as 1.57 S cm^{-1}. The Co-HAB displayed outstanding chemical stability in both aqueous and organic media and thermal stability to 300 °C. This system presents a promising new electrode material for sodium-ion storage [4]. In this approach, the 2D conducting MOFs constructed with flat organic linkers like HITP=2,3,6,7,10,11-hexaiminotriphenylene), H_4TTFTB = tetrathiafulvalene tetrabenzoate, 2,5-disulfhydrylterephtalate (DSBDC) etc. could give conductivities up to 100 S cm^{-1} [5]–[7]. Despite the fact that these methods have occasionally produced MOFs with significant electrical conductivity and intact porous structure, however only a few MOF building blocks with necessary charge-transport properties are currently available. Therefore, these techniques limit the use of wide variety of structures and properties of available conventional MOFs. Another approach is to infiltrate the MOF with conductive materials like carbon compounds, metal nanoparticles, metal oxides, conducting polymers to give a conductive composite. Kitagawa et al. have considered the infiltration MOFs with vinyl polymers like polypyrrole (PPy), polythiophene (PTh) to increase the electrical conductivity [8]. When the polymers are prepared ex-situ and tried to be incorporated into the framework, they resulted in composites of MOF with the grafted polymer chains on

their framework, or MOFs in a polymer matrix. On the other hand, by loading the monomers into the pores of MOF and post-polymerization by adding reducing agent may generate a pore filled conducting polymer@MOF. Many MOF based composites have also been explored by introducing carbon nanotubes, graphene, 3D carbons into the MOF framework to obtain conductivity. It is very challenging to fill these nanocarbons into the MOF pores through bottom-up methods of deposition as it requires harsh conditions that would damage the MOFs structure partly or fully [9].

Although extrinsically conducting MOFs can be generated using a variety of readily available SBUs by this post synthetic modification strategy, their structural stability in aqueous conditions is the main barrier to their implementation in electrochemical processes. To address this issue specific strategies have been employed to design stable MOFs, in which a zirconium (Zr) based MOF is obtained via strong hard-acid hard-base coordination bond between Zr atom and benzenedicarboxylic (BDC) ligand [10] . Functionalizing UiO-66 with different functional groups such as -SH, NH_2 etc. has led to proton conductivity up to 10^{-1} S cm^{-1} according to various studies. Y. Q. Lan et al. have functionalised UiO-66 with NH_2 and AS (amino and sulphonic acid groups) through condensation reaction with imidazole-2-carboxylate to bind imidazole (IM) to the framework. They succeeded in getting highly stable proton conducting MOF with a conductivity value of 1.54×10^{-1} S cm^{-1} [11]. Nevertheless, extensive investigation of electronic conductivity in UiO-66 MOF along with relevant transport mechanism is yet to explore.

Inspired by the reported works, here UiO-66 has been worked out by adding several guests like silver oxide nanoparticles (Ag_2O NP) and conducting polymer poly(3,4-ethylenedioxythiophene) (PEDOT) into the pores of UiO-66 MOF. In the first work, Ag_2O was incorporated into UiO-66 through two different approaches. In the former approach Ag_2O was loaded to the framework by mixing the precursor $AgNO_3$ with as prepared UiO-66 in solvent acetonitrile without adding any reducing agent. The $AgNO_3$ infiltrated inside the pores of UiO-66 are then reduced to Ag and Ag_2O NPs on treatment with acetonitrile, the sample being labelled as S1(MOF). In another approach, a natural reducing agent has been employed to incorporate Ag_2O into the UiO-66 framework. This reducing agent was

obtained from the banana root bulb (BRB) by boiling it in deionised (DI) water. The extract so obtained was stored at a temperature of 4 ° C. This BRB extract was utilised to modify UiO-66 post-synthetically by adding Ag_2O NPs to the framework designated as S2(MOF). As for PEDOT@UiO-66 framework in-situ polymerization of EDOT was performed by allowing UiO-66 to soak EDOT followed by adding of $FeCl_3$ to the mixture. In order to evaluate the structural and morphological characteristics following modification with the guest molecules, the as-prepared MOF samples were examined using XRD, FTIR, TEM, FESEM, N_2 adsorption-desorption isotherm, and Raman spectroscopy.This chapter discusses the structural, morphological and vibrational features of Ag_2O incorporated UiO-66 MOFs (Ag_2O@UiO-66: S1(MOF) and S2(MOF)) and PEDOT inserted UiO-66 MOF (PEDOT@UiO-66), on a comparative basis.

3.2 Structural and morphological investigation of Ag_2O@UiO-66 MOFs

3.2.1 Structural characterization

The structures of as-prepared samples were first characterized for the confirmation of structural stability of UiO-66 and loading of NPs. The powder-XRD of S1(MOF) and S2(MOF) samples were compared with the host UiO-66, as shown in Fig. 3.1 (a). The XRD patterns of both S1(MOF) and S2(MOF) keep UiO-66 peaks intact which are positioned at, 2θ = 7.3°, 8.5°, and 25.6°. There are a few low intense additional peaks (2θ = 32.8 and 45.6°) present in the diffractogram of S1(MOF) which can be attributed to the (111), and (200) planes of Ag_2O NPs as identified from the JCPDS Card No. 41-1104 [12]. The diffractogram of S2(MOF) has a poorly resolved peak at, 2θ = 32.8° due to the low yield of Ag_2O NPs realized through the natural extract of BRB.

The FT-IR spectra of Ag_2O, UiO-66, S1(MOF) and S2(MOF) where Ag_2O NPs exhibit stretching vibrational bands in the range of 600 cm^{-1} to 900 cm^{-1} can be found in Fig. 3.1(b). To be mentioned, inorganic compounds due to their higher atomic masses would show low frequency peaks as compared with organic, lighter species. The broad peak in the pattern of Ag_2O NPs is due to the combination of two bands ascribed to the stretching and bending of Ag-O and Ag-O-Ag [13].

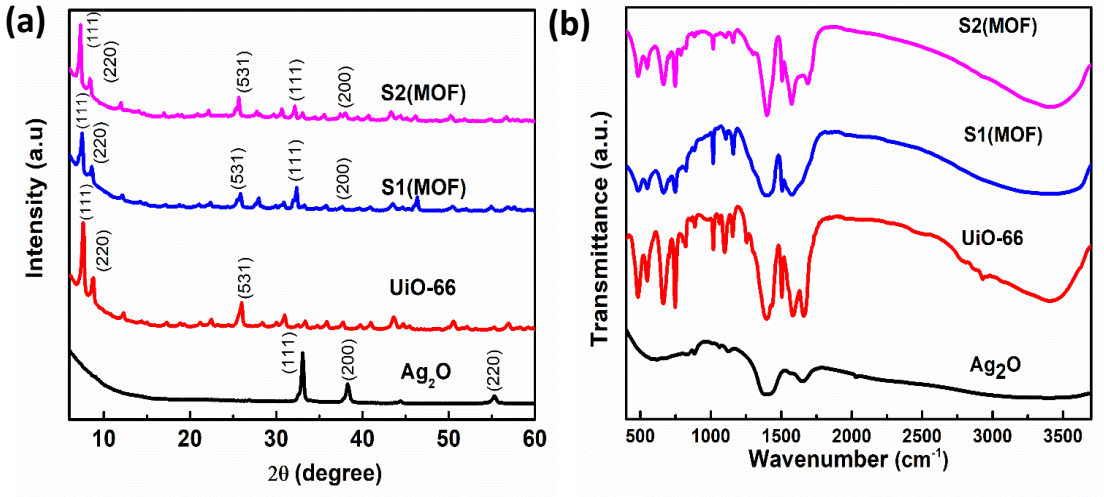

Fig. 3.1 (a) The PXRD pattern of Uio-66, S1(MOF) and S2(MOF) (b)FT-IR spectra of Uio-66, Ag_2O, S1(MOF) and S2(MOF).

In the spectra of the host UiO-66 numerous sharp absorption peaks can be witnessed located at 1676 cm^{-1}, 1584 cm^{-1}, 1504 cm^{-1} to 1394 cm^{-1} and corresponded to the symmetric and asymmetric stretching modes of C=C and C=O bonds of carboxylate group of the linker BDC [14].These modes are observed in the spectra of both Ag_2O loaded UiO-66 samples suggesting adequate structural stability of UiO-66. Along with those, peaks at lower wavelength regions are ascribed to the in-plane and out-of-plane C-H bending modes of benzene ring in the BDC. Moreover, the weakly resolved peaks due to Ag_2O at ~889 cm^{-1} and 1147 cm^{-1} have appeared in the spectra of S1(MOF) and S2(MOF) which infer the presence of Ag_2O in the systems under study.

3.2.2 Morphological Characterization

3.2.2.1 Field emission scanning electron microscopy

The morphological studies of UiO-66, Ag_2O, S1 (MOF) and S2 (MOF) can be revealed through FESEM imaging, as shown in Fig. 3.2. As expected UiO-66 is seen to have a morphology similar to spheroids where particles are closely aggregated. The particles have a smooth surface with average size ranges between 100-150 nm. Fig. 3.2 (b) shows the morphology of Ag_2O NPs prepared for a comparative study. In Fig. 3.2 (c) the S1(MOF) shows spheroid entities whose size and shapes are like those of pristine UiO-66 with non-

traceable smaller particles over the surface of UiO-66 particles. This suggests that Ag_2O NPs are not present on the exterior and that they may be present within UiO-66's micropores. While S2 (MOF) has NPs implanted all over the surface of the UiO-66 MOF, as seen in the Fig. 3.2 (d). The morphology of UiO-66 remained same in S2(MOF) with homogeneously distributed Ag_2O NPs over the particle surface. The presence of Ag_2O NPs in the composites can also be ensured by energy dispersive x-ray spectroscopy (EDX) as the spectra provided the elemental indicators of Ag_2O along with Zr, C and O (Fig. 3.2 (e) and (f)).

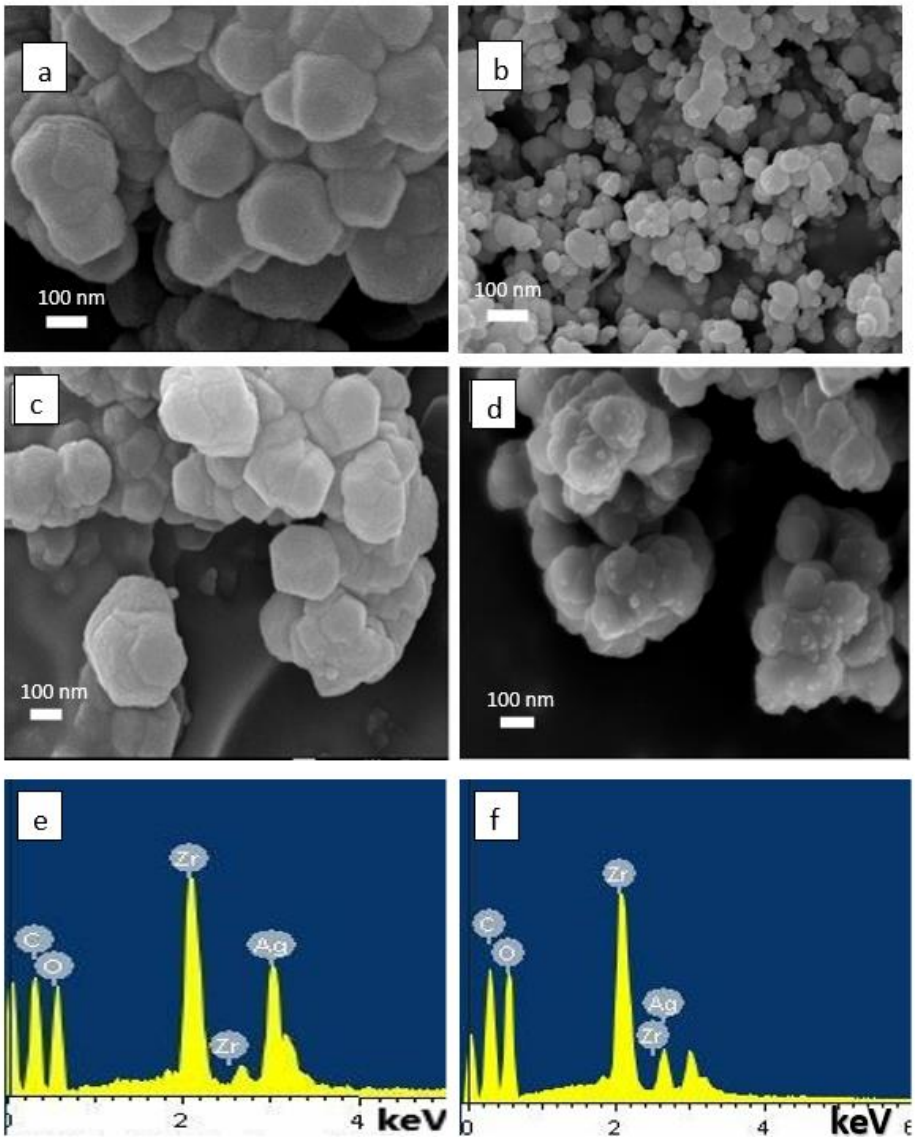

Fig. 3.2 Scanning Electron Microscopy (SEM) images of (a) UiO-66 (b)Ag_2O (c) S1(MOF) (d) S2(MOF), (e) EDX of S1(MOF) (f) EDX of S2(MOF).

(a) S1(MOF)

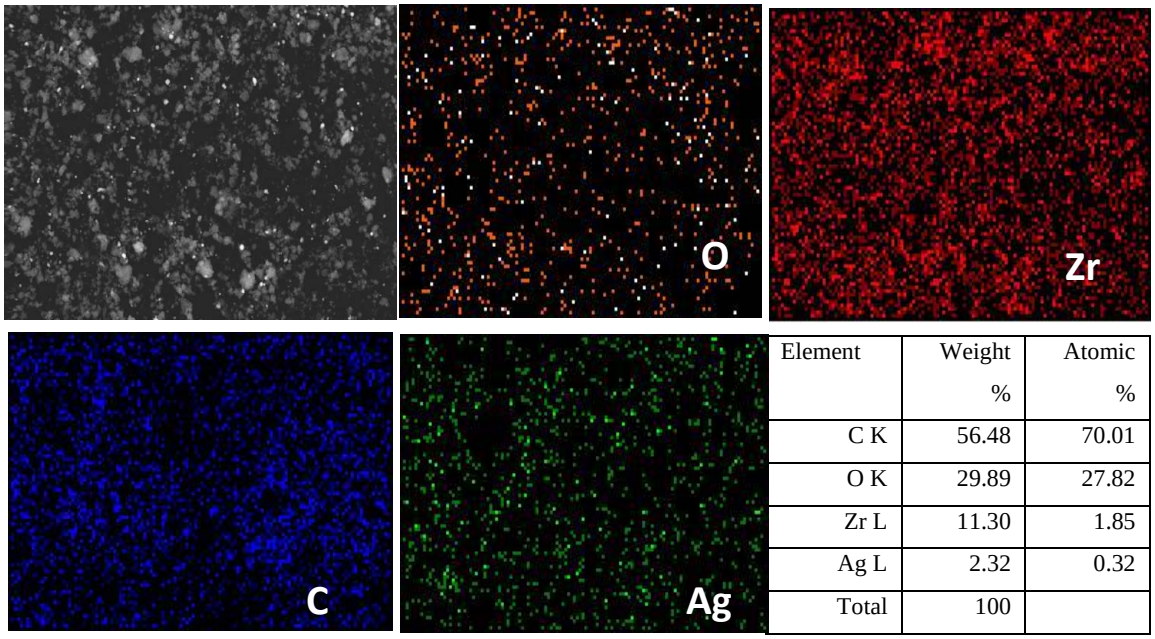

Element	Weight %	Atomic %
C K	56.48	70.01
O K	29.89	27.82
Zr L	11.30	1.85
Ag L	2.32	0.32
Total	100	

(b) S2(MOF)

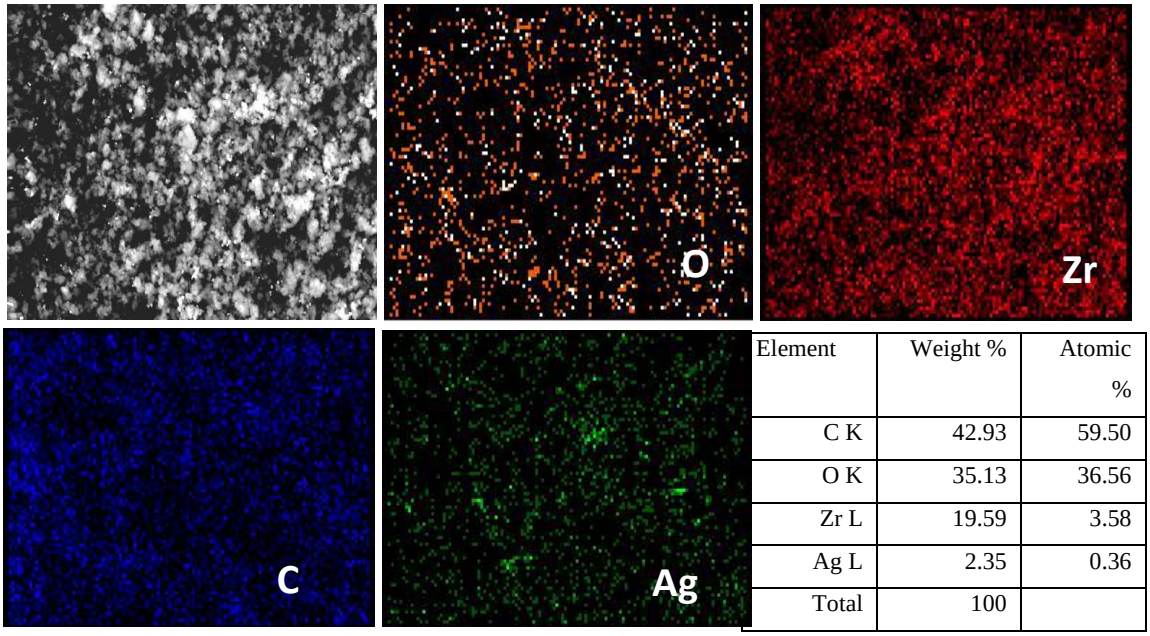

Element	Weight %	Atomic %
C K	42.93	59.50
O K	35.13	36.56
Zr L	19.59	3.58
Ag L	2.35	0.36
Total	100	

Fig. 3.3 (a) Elemental mapping of S1 (MOF) and composition of different element (b)Elemental mapping of S2 (MOF) and composition of different elements.

Analysis of elemental composition through elemental mapping gives an idea on quantifying Ag in both the composites, which estimates comparable values (Fig. 3.3 (a), (b)). This leads to a conclusion that the Ag_2O NPs were either implanted somewhere inside the pores of MOF, or present over the surfaces of UiO-66 in S1(MOF) and S2(MOF), respectively.

3.2.2.2 Transmission electron microscopy

To acquire a better insight into the distribution of Ag_2O NPs in the MOF microstructure, TEM imaging of S1(MOF) and S2(MOF) were performed and depicted in Fig. 3.4 (a-f). The TEM images of S1(MOF) in two different scale values can be found in the upper panel, Fig. 3.4 (a), (b). The image shows agglomerated octahedral shaped particles of size ranging 40-60 nm. The UiO-66 particles has some darker spots in their structures which could be identified as the Ag_2O NPs. Since the Ag_2O NPs are present in the pores of UiO-66 (as assumed by FESEM imaging), the particles are not properly resolved in TEM images. However, EDX analysis presented in Fig. 3.4 (c) revealed distinct peaks corresponding to silver, confirming the elemental presence of Ag within the MOF structure. This conclusive evidence supports the hypothesis that Ag NPs are incorporated within the MOF, despite their lack of visibility in the TEM images. Additionally, the SAED in Fig. 3.4 (g) patterns displayed characteristic crystallographic planes from both the MOF and the Ag NPs, indicating adequate incorporation and retention of the nanoparticles within the porous framework. Whereas, in S2(MOF) Ag_2O NPs are clearly visible in the images Fig. 3.4 (d), (e). In these images spherically shaped Ag_2O NPs of average size ~ 20 nm are found to be available outside the UiO-66 octahedral cavities. In this case also UiO-66 particles are seen to have an aggregation of particles of size ranging 40-50 nm. Here also, EDX data Analysis of TEM images ensure the findings of FESEM characterization as depicted in Fig.3.4(f). Additionally, the SAED pattern evidences the coexistence of crystallographic planes of UiO-66 and Ag_2O, providing confirmation of NP inclusion in the framework presented in Fig.3.4 (h) [15][16]. The use of natural extract has given rise to Ag_2O NPs of bigger size which could be the reason of finding them outside the MOF pores with diameter in the microporous range.

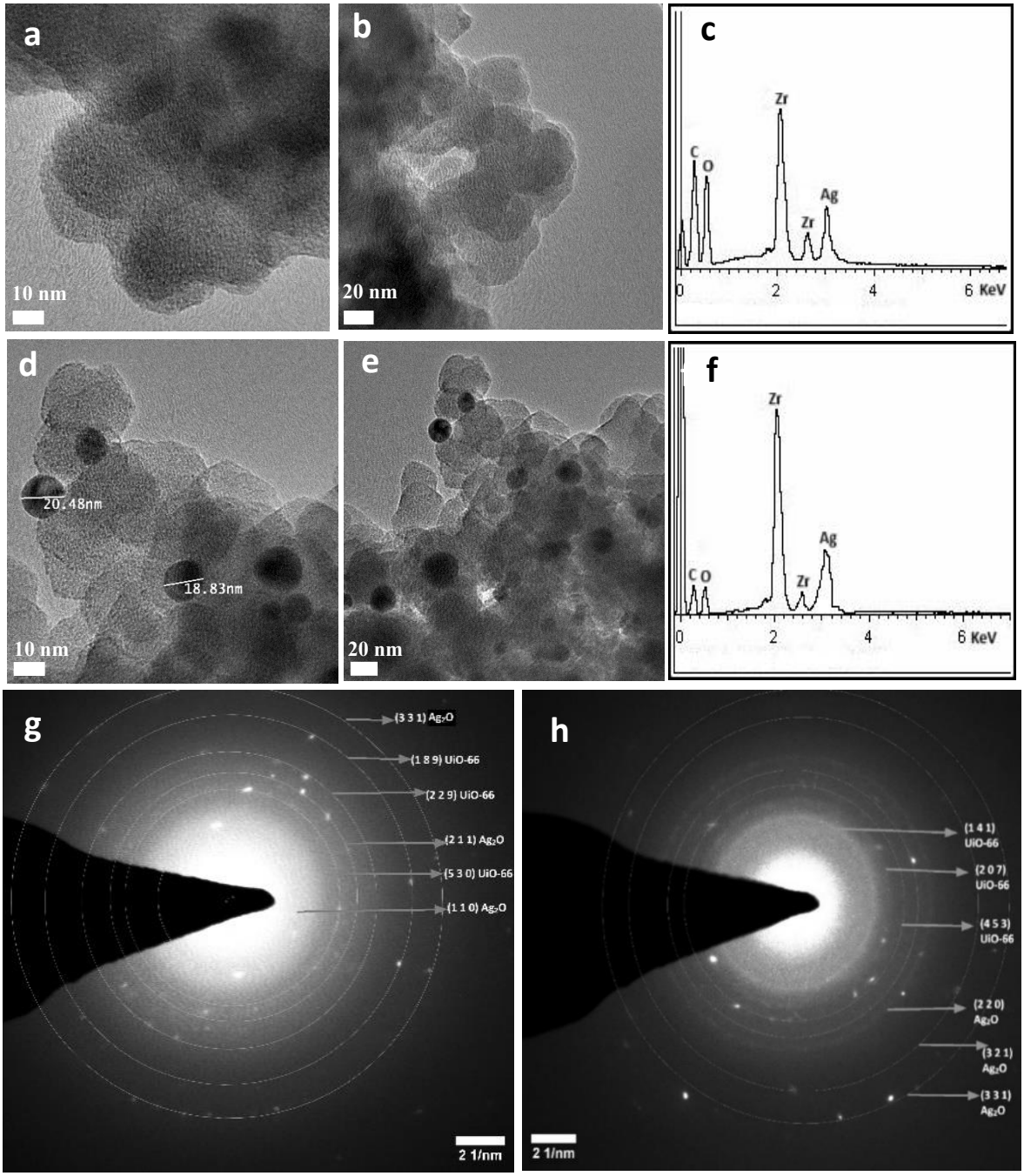

Fig. 3.4 Transmission Electron Microscopy (TEM) (a),(b) S1(MOF) at different magnifications and (d), (e) S2(MOF) at different magnifications. (g) and (h) SAED pattern and (c) and (f) EDX of S1(MOF) and S2(MOF), respectively.

3.2.3 BET surface area and pore size distribution

N_2 adsorption isotherm of UiO-66, S1(MOF) and S2(MOF) taken at 77 K are shown in Fig. 3.5 (a). The isotherms of UiO-66 and S1(MOF) are type-I indicative of microporous nature of the materials [17]. However, the amount of N_2 adsorbed by S1(MOF) is smaller than UiO-66, which is the proof that Ag_2O NPs have already occupied the micropores. The isotherm of S2(MOF) is type-IV according to the IUPAC classification related to the mesopores [18]. The hysteresis observed at higher partial pressure has a H1 shape. According to IUPAC, type H1 is frequently related to porous materials with agglomerates of roughly homogeneous spheres or well-defined cylindrical-like pore channels. The S2(MOF) with Ag_2O particles spread over the UiO-66 crystals results into aggregation of spherical particles which may block the original octahedral/tetrahedral pores of UiO-66 and with the agglomeration offers mesopores on the surface. These results were assisted with the pore size distribution analysis shown in Fig. 3.5 (b). Using H-K method it was observed that UiO-66 has two types of pores, octahedral of size ~ 16 Å and tetrahedral of size ~ 10 Å which got partially filled with Ag_2O when infiltrated in S1(MOF). The size of the pores reduced to 9.5 Å and 13.2 Å as depicted by the pore size distribution. On the other hand, the S2(MOF) system exhibits a very low differential pore volume with the radii of ~ 12 Å and 24 Å. The specific surface area can be calculated by using the following formula-

$$S_{BET} = \frac{v_m NA}{M \text{x} 22400} \tag{3.1}$$

where S_{BET} is the specific surface area, N is the Avogadro's constant, A is the cross-section area of the adsorbate molecule and M is the mass of the test sample and v_m is the volume of N_2 adsorbed at monolayer coverage. The value of v_m was obtained from the slope and intercept of the plot that fits the BET equation [19] -

$$\frac{1}{v\left[\left(p_o/p\right)-1\right]} = \frac{C-1}{v_m C}\left(\frac{p}{p_o}\right) + \frac{1}{v_m c} \tag{3.2}$$

Table 3.1. Microporous properties of UiO-66, S1(MOF), S2(MOF) systems

Samples	BET surface area S_{BET} (m^2/g)	Total pore volume measured at $\frac{P}{P_o} = 0.99$ v (cc/g)	The pore diameter calculated using H-K method. D (Å)
UiO-66	835.703	0.016	16.11 and 10.7
S1(MOF)	708.128	0.009	13.2 and 9.5
S2(MOF)	873.982 m^2/g	0.102	24.56 and 12.7

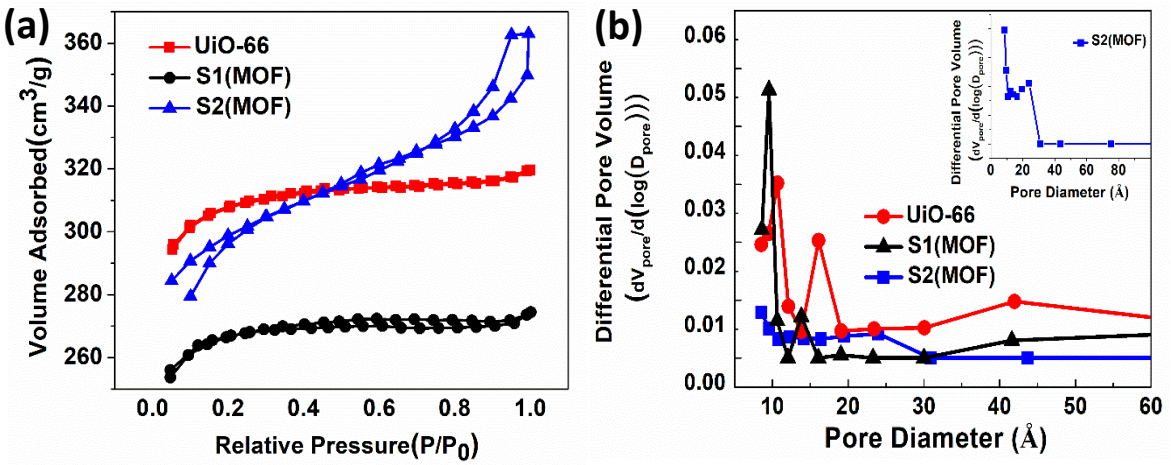

Fig. 3.5 (a) N_2 adsorption-desorption isotherm of UiO-66, S1(MOF), S2(MOF) (b) H-K pore size distribution of UiO-66, S1(MOF), S2(MOF); inset magnified view of S2(MOF).

where, p is the equilibrium pressure, p_o is the saturation pressure, v is the volume adsorbed at p C is the constant. The S_{BET} values corresponding to present studies are presented in Table 3.1. The UiO-66 MOF is widely recognised for having a large specific surface area, which is preserved in this case as well. After loading Ag_2O in the micropores of UiO-66 in S1(MOF), there is an obvious decrease in S_{BET} observed, whereas, in the S2(MOF) the S_{BET} is quite close to the host UiO-66. As a result, anchoring Ag_2O into the surface of UiO-66 does not influence the active surface area.

3.3 Structural and morphological analysis of PEDOT@UiO-66

3.3.1 Structural features

Technically, the encapsulation of PEDOT within the UiO-66 micropores has progressed through two important steps. First, activation of UiO-66 by preheating and then exposing to liquid monomer EDOT to facilitate in-situ polymerization of PEDOT in restricted volume, within the pores. Later, the EDOT adsorbed UiO-66 was mixed with ethanolic solution of oxidising agent $FeCl_3$ following an earlier work [20]. A grey-coloured powder is yielded by taking 90 (w/w) % of UiO-66: EDOT ratio in ethanol for polymerization with $FeCl_3$. The powder X-ray diffraction (P-XRD) studies of UiO-66, before and after PEDOT insertions, were compared with the diffractogram data of PEDOT (Fig. 3.6). Observably, adequate crystallinity of the PEDOT polymerised MOF was retained as characterized by the prominent peaks at, $2\theta = 7.35^{o}$ (111), $2\theta = 8.48^{o}$ (220), $2\theta = 25.6^{o}$ (531) as evident from Fig. 3.6. A slight shifting in peak positions from $2\theta = 7.35^{o}$ to 7.23^{o} and $2\theta = 8.48^{o}$ to 7.96^{o} in the nanocomposite is an indicative of homogeneous compression of lattice planes of UiO-66 due to insertion and segregation of a new material into a regular, periodic lattice. Nevertheless, the relative intensities of the peaks of bare, and PEDOT inserted MOFs are quite different due to the lowering of crystallinity caused by the presence of polymeric conformation in the micropores.

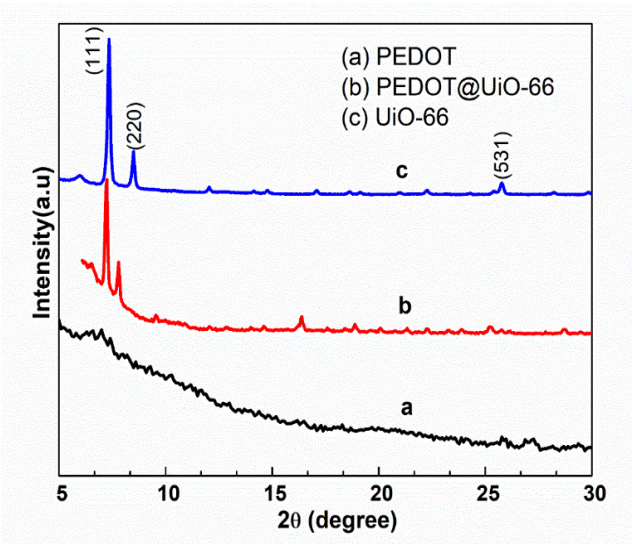

Fig. 3.6 X-ray diffractograms of PEDOT, PEDOT@UiO-66, and UiO-66 MOF systems.

3.3.2 Morphological features

3.3.2.1 Transmission electron microscopy

The morphological features of the UiO-66 and PEDOT@UiO-66 MOFs were obtained on a TEM operating at an accelerating voltage of 200 kV (Fig. 3.7). Although there is a slight departure from the regular octahedral structure, the UiO-66 exists in a spheroidal morphology as visualized in the TEM images [21]. The selected area electron diffraction (SAED) pattern of UiO-66 presented in Fig3.7 (c) suggests the polycrystalline nature of the synthesised MOF, with the presence of crystalline planes such as (0 7 0) corresponds to d-spacing of 1.9645 Å. Additionally, the EDX analysis depicted in Fig.3.7 (d) and detailed in table (i) reveals the elemental composition of the constituents of UiO-66 such as C, O and Zr. Interestingly, after inclusion of the guest polymer into the MOF, octahedral morphology remained intact as can be witnessed from the images, Fig. 3.7s (c) and (d). It should be noted that although the TEM pictures do not clearly show polymerization inside the pores, it must have happened partially because the MOFs' surface does not show any signs of rough or fibre-like aggregates. On the other hand, the presence of all the elements of PEDOT with homogeneous spread among the MOF networks can be affirmed from the energy dispersive X-ray spectroscopy (EDX) indicating sulphur (S) and zirconium (Zr) as the elemental markers for the PEDOT and UiO-66; respectively (Fig 3.7 (f)). Moreover, the SAED pattern of PEDOT@UiO-66 presented in Fig.3.7 (e) reveals that the crystalline structure of the MOF is preserved after polymerization of PEDOT. SAED analysis provides insights into the crystallography of UiO-66, revealing the presence of several significant planes, including (2 1 1), (3 0 2), and (1 1 3) [15]. These planes are indicative of the ordered arrangement of atoms within the UiO-66 crystal structure. Being amorphous in nature no crystalline plane corresponding to PEDOT.

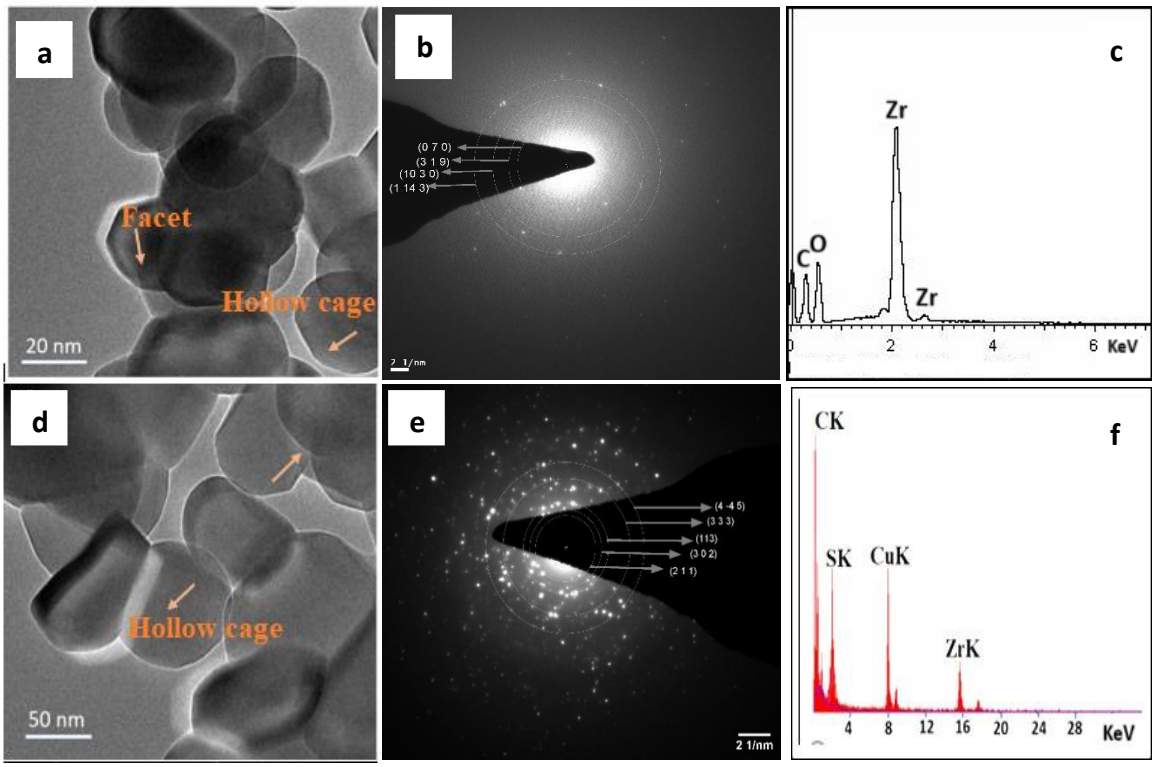

(i)

Element	Weight %	Atomic %
C K	44.61	61
O K	34.28	35.19
Zr L	21.80	3.80
Total	100	100

(ii)

Element	Weight %	Atomic %
C K	60.98	67.80
O K	38.78	32.03
Zr K	0.22	0.09
S K	0.21	0.03
Cu K	0.22	0.05
Total	100	100

Fig. 3.7 (a) TEM images, (b) SAED pattern and (c) EDX spectra of UiO-66 MOF. (d) TEM images, (e) SAED pattern and (f) EDX spectra of PEDOT@UiO-66. Elemental composition of UiO-66 (i) and PEDOT@UiO-66 (ii)

3.3.2.2 Field emission scanning electron microscopy

The FESEM images of UiO-66 and PEDOT@UiO-66 at different magnifications are presented in Fig. 3.8. The shape of UiO-66 MOF is largely spheroidal in shape with particle size ranging 100-150 nm. The images of PEDOT@UiO-66 are seen to be fragmented from spheroids to smaller spheres of dimension 70-100 nm. It is composed of UiO-66 particles of nearly same size as the parent MOF as well as some fragmentation of it.

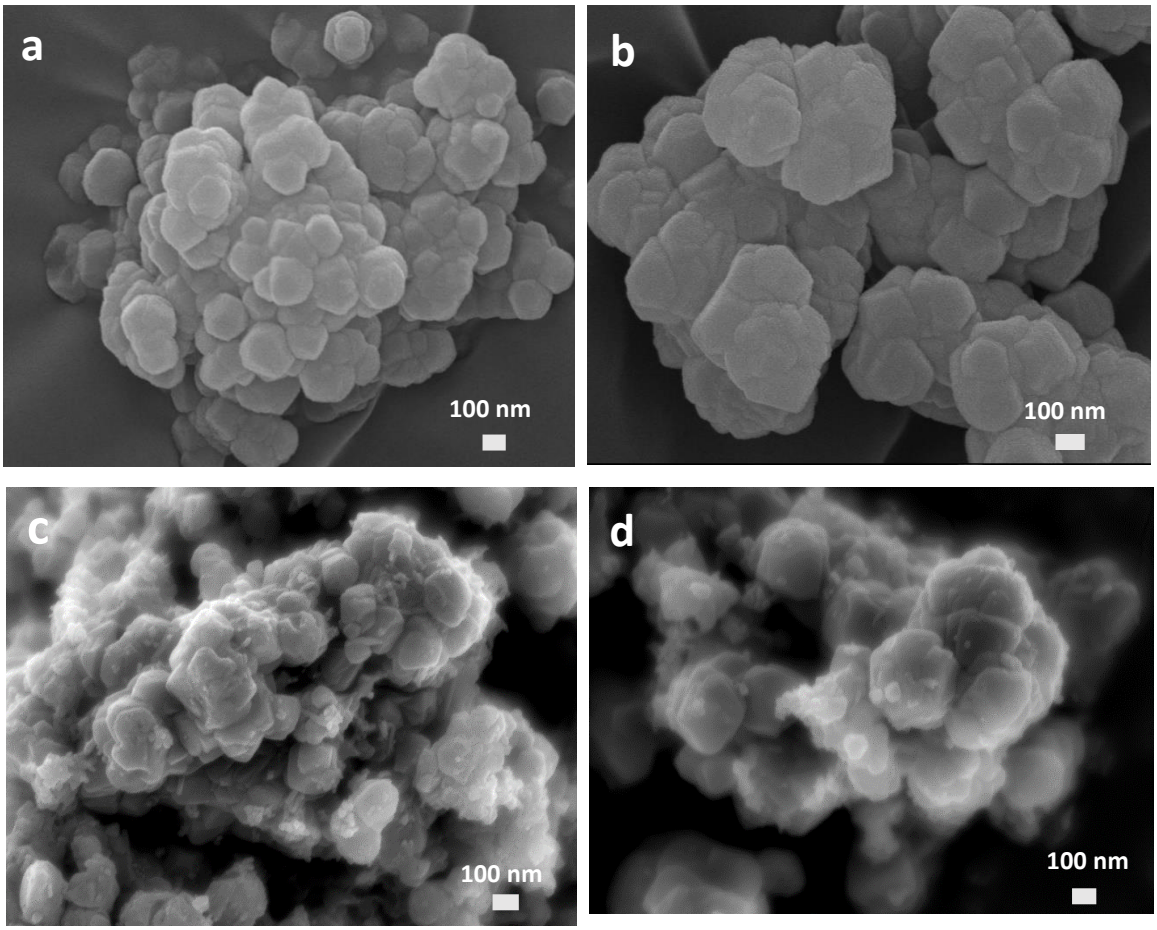

Fig. 3.8 FESEM images of UiO-66 at (a) 40 kX (b) 50 kX and PEDOT@UiO-66 66 at (c) 40 kX (d) 50 kX.

The fragmentation may have occurred due to the chemical treatment during the polymerization of PEDOT inside the pores. The structure exhibits no degradation as seen in the XRD data, maintaining the phase of UiO-66 intact, but the strength of the characteristic peaks has dropped, which can be attributed to the fragmented morphologies of the PEDOT@UiO-66 system. Moreover, particles are seen to have a larger agglomeration in PEDOT@UiO-66 material possibly because of the presence of polymer in the framework

3.3.3 BET surface area and pore size analysis

Surface area and pore size of the bare, and PEDOT@UiO-66 MOFs were determined by nitrogen adsorption/desorption mechanism and at a temperature of 77 K (Fig. 3.9 (a-d)). Featuring type-I isotherm, the pristine MOF system was believed to have numerous micropores [32]. Moreover, the PEDOT@MOF exhibits an altered, yet type-I isotherm characterizing microporous nature of the composite formed (Fig. 3.9 (c)). Not surprisingly, a decline trend of the N_2 uptake of the composite system as compared to the pristine MOF, would suggest the presence of PEDOT filled micropores. Considering in Fig 3.9 (a) and (b), the surface area S_{BET} was calculated using equation (3.1) and (3.2). Here, the UiO-66 MOF offered a typical value of S_{BET} as, 1057.6 m^2/g which is in good agreement with the reported one [22] . However, the PEDOT@UiO-66 MOF showed a lowered S_{BET} of 743.57 m^2/g as compared to the pristine MOF due to partially filled micropores with the polymeric entities. To be mentioned, although the surface area of the UiO-66 is lowered by nearly 29.6% upon PEDOT insertion in the pores, the overall microporous network of the MOF composite remains intact with plentiful unfilled sites. This accounts for partial polymerization has been taken place inside the pores of UiO-66.

The micropore size distribution was determined using Horvath and Kawazoe (H-K) method, which reveals two kinds of micropores as indicated by two sharp peaks at ~8 Å and ~12 Å, and attributed to tetrahedral and octahedral pore geometries, respectively and shown in Fig. 3. 9 (d) [23]. In the PEDOT@MOF composite, there exists a sharp peak at ~8 Å with low differential pore volume and a broad peak that spreads over the range of 13-30 Å. Unquestionably, this observation depicts that the PEDOT is mainly accommodated in the octahedral pores while the peaks of tetrahedral pores remained almost unaltered. Since the tetrahedral pores are smaller in size the accommodation of monomer along with the oxidative agent were not allowable and could give rise to the maximal unfilled sites even after the polymerization. Upon deconvolution of the asymmetrically broadened feature at ~13-30 Å, one could recover two peaks at ~14.9 Å and 21.3 Å indicating adequacy of additional pores of varied dimensions. It may be worth mentioning here that, ~96% of the tetrahedral and 70% of octahedral pore volumes remained unfilled with the incorporation PEDOT in the MOF host. An illustration in

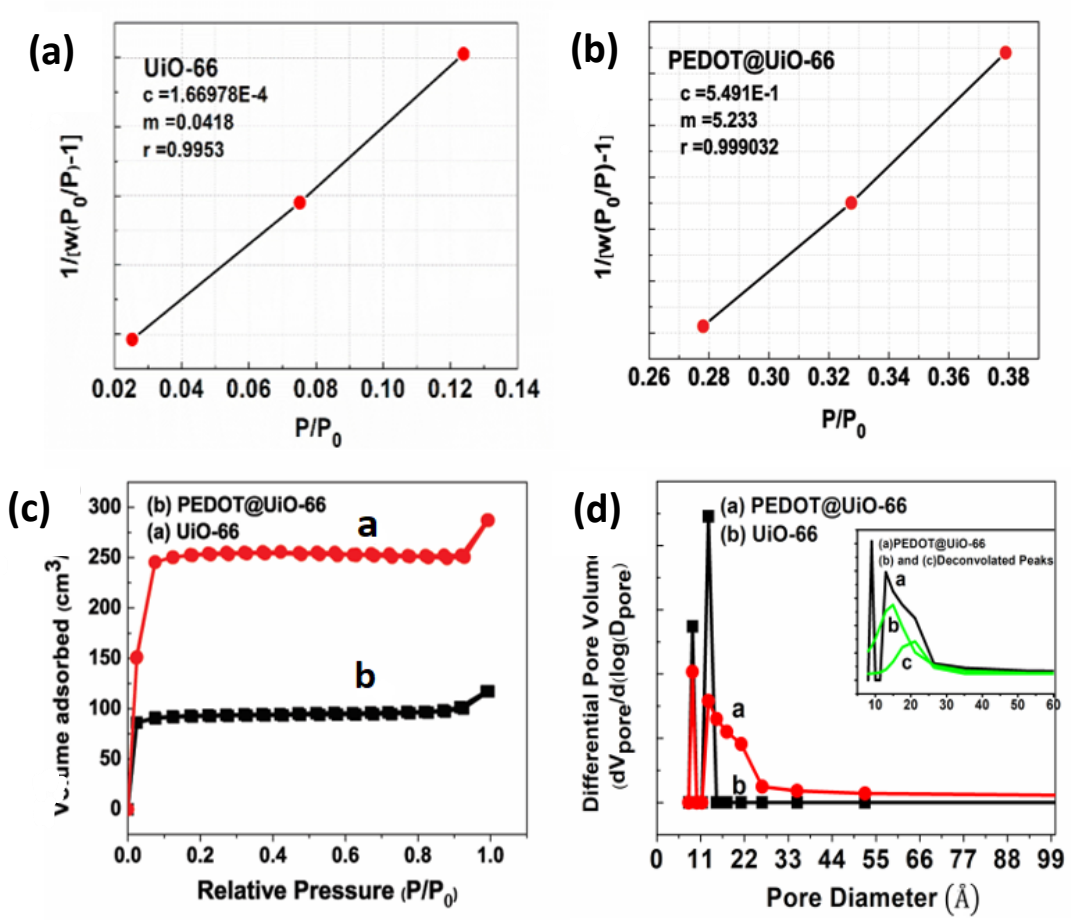

Fig. 3.9 BET surface area plots of (a) UiO-66 MOF, and (b) PEDOT@UiO-66 MOF composite. N_2 adsorption/desorption isotherm of (c) UiO-66, and PEDOT@UiO-66, and (d) HK method employed to reveal pore size distribution present in the studied systems.

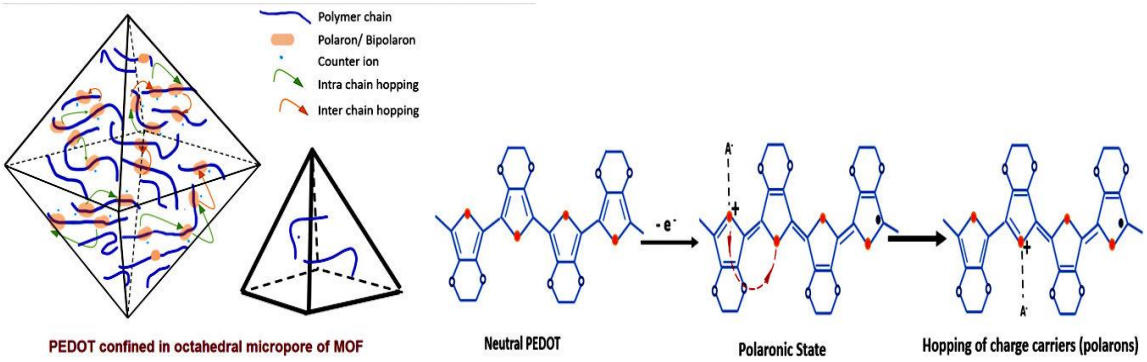

Fig. 3.10 PEDOT polymeric chains occupying hugely in the octahedral pore and feebly within the tetrahedral pore of the UiO-66 MOF. From charge neutral to hopping transport due to delocalization of electrons as well as the creation of bipolarons are also shown in the adjacent scheme.

support of the micropore filling of PEDOT into the MOF host along with bipolaronic state can be found in Fig. 3.10.

3.3.4 Molecular stretching and Raman active modes

In UiO-66 MOF the linker HCOOH forms a dimer with two hydrogen bonds and has a centre of symmetry and consequently, it gives rise to symmetric and asymmetric stretching vibrations. While the symmetric vibration is Raman active, asymmetric one corresponds to IR active mode [24]. The C=C bond in terephthalic linker of the MOF has a symmetric stretching mode at, ~1608 cm^{-1} and an asymmetric stretching mode at 1662 cm^{-1} (Fig. 3.11 (a) and (b)). On the other hand, the carboxylic group C=O has both symmetric and asymmetric stretching modes, indicated by two intense bands at ~1399 and 1579 cm^{-1}. In the region between ~1000 to 1250 cm^{-1} there exist several weak absorption peaks assigned to C-O stretching vibrations, coupled with C-C stretching overtones. Intense bands located at ~664 and 748 cm^{-1} are due to the out-of-plane bending of =C-H which represent the mono-substituted benzene ring with carboxyl groups in BDC [25]. In-plane C-H bending vibrations are probed in the region of ~1000- 1300 cm^{-1} being overlapped with other absorption features. The μ_3-OH stretch and the μ_3-O stretch of UiO-66 can be recognized from the bands of ~484 and 548 cm^{-1} (typically, 60 meV), respectively.

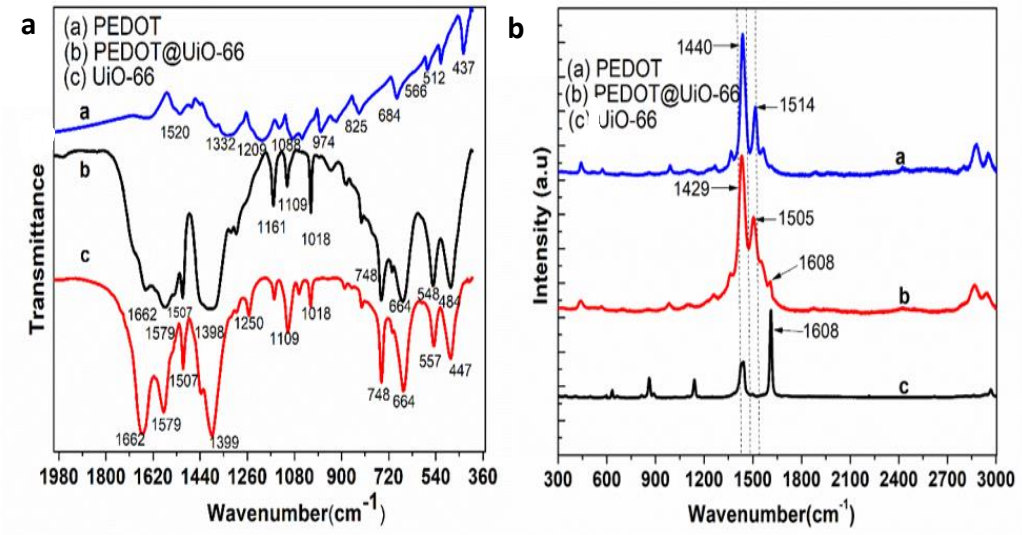

Fig. 3.11 (a) FTIR, and (b) Raman spectra of the investigated systems PEDOT, PEDOT@UiO-66 composite and UiO-66 MOF systems.

Additional intense bands at ~1507 cm^{-1} arise in the spectra of PEDOT@UiO-66 MOF and can be assigned to the asymmetric C=C stretching mode of ethylenedioxy group. The poorly resolved absorption peaks are positioned in the range 800-1000 cm^{-1} depicting stretching vibrations of the C-S-C bonds [26]. Interestingly, several peaks in the spectra of nanocomposites are broadened due to the overlapped absorption peaks of both PEDOT and UiO-66. The change in conformation of PEDOT after polymerisation within the micropores of UiO-66 can be evaluated through Raman spectroscopy (Fig. 3.11 (b)). To be mentioned, the PEDOT in its doped states offer two resonating structures: benzoid and quinoid. Conjugated bonds present between the C_α= C_α and C_β= C_β in the quinoid conformation can make it linear while the benzoid is a coiled conformation with C_α= C_β. It gives a high conjugation in the chain backbone of quinoid structure making it rigid and allows a strong interaction between the chains of PEDOT for a higher mobility [27]. The spectra of bulk PEDOT, UiO-66 and PEDOT@ UiO-66 MOF were recorded on a Raman spectrometer (Renishaw, UK) equipped with a ~514 nm line of 50 mW He-Ne laser source. The spectra for PEDOT@UiO-66 MOF consisted of peaks corresponded to both the MOF and PEDOT systems. The peak at ~1608 cm^{-1} characterizes symmetric stretching modes of O=C-O of the BDC linker which was also present in the spectra for the composite with a red shift. In the Raman spectra of PEDOT, the peak of interest is at ~1440 corresponds to C_α=C_β symmetric stretching modes [28], which is red shifted and becomes narrow when coexisted with that of the MOF host. Apparently, this red shift is the indicator for benzoid-to-quinoid transformation [29]. Less intense peaks positioned at ~1366 cm^{-1} and 1260 cm^{-1}, are associated with C_β-C_β and C_α-C_α stretching vibrations; respectively. Notably, the asymmetric stretching of C_α=C_β which would split into two peaks at ~1505 cm^{-1} and 1568 cm^{-1} were seen to be shifted towards higher wavenumber in the composite system. Thus, benzoid-to-quinoid transformation occurs when radical is formed on the molecule upon oxidation. In fact, the EDOT was introduced to a new environment of Zr^{2+} ions and organic part with polar groups of UiO-66 MOF along with the oxidizing agent $FeCl_3$ which led to the doping of PEDOT. A neutral PEDOT has a benzoid structure with C_α=C_β bond having two conjugated π-electrons while doped PEDOT can have a quinoid resonant structure with no π conjugated electron in C_α-C_β [30]. It may be worth mentioning here that, due to

a conformational change of the polymer, the number of delocalized electrons in the backbone will increase which eventually enhance the conductivity of PEDOT.

3.4 Conclusion

In this chapter two composites of UiO-66 have been discussed- first is Ag_2O nanoparticle loading in the UiO-66 framework and the second PEDOT incorporated in UiO-66 framework. Structural and morphological investigation of Ag_2O loaded UiO-66 has been done with care. Two samples of Zr-based MOF UiO-66 and Ag_2O NPs have processed via two different synthesis routes. In the former route conventional strategy was employed to reduce the Ag_2O with the help of acetonitrile while the later route involved a natural reducing agent extracted from the banana root bulb (BRB). In both the samples structure of UiO-66 remained intact after post-synthetic modification. Infact, Ag_2O NPs were loaded into the UiO-66 framework following two distinct routes. In the first sample S1(MOF), the size of the silver NPs was small enough to make their ways into the micropores of UiO-66 host without lying over the MOF surfaces. In S2(MOF), however, Ag_2O NPs were apparently seen over the surfaces of the MOF particles. From the structural and morphological investigation it was confirmed that Ag_2O NPs were efficiently incorporated into UiO-66 structure without much hammpering the crystallinity of the parent MOF. However, the Ag_2O NPs have occupied distinct spaces, such as pores and surfaces of the host UiO-66.

The structural, morphological and vibrational aspects of PEDOT inserted Uio-66 were discussed. It demonstrated the effective polymerisation of PEDOT within the micropores of UiO-66 MOF and characterized through XRD, FTIR, EDX and BET analyses. While the TEM study provided information about the smooth morphological characteristics of PEDOT@UiO-66, EDX analysis was considered to confirm the presence of PEDOT. The FT-IR results helped to observe the chemical changes occurred in the nanocomposite as the C, S, O of thiophene rings were in a different environment in comparison to the bare PEDOT counterpart. The nanocomposite has broadened peaks, which specify possible interaction between the metal ions, or components of the linker with the fragments of PEDOT. Moreover, N_2 adsorption-desorption isotherms allowed us to infer partial incorporation of the polymer in the micropores quite selectively. The

conformational change due to the entrapped PEDOT was evident from the shifting of the Raman peak towards high frequency side while indicating benzoid to quinoid transformation. In the benzoid conformation, C_α-C_α has a sigma bonding, whereas in quinoid conformation these carbons have a π-bond. This means quinoid conformation has a higher density of π-electrons that can easily be delocalized over the whole chain so that PEDOT holds a higher carrier mobility, and hence enhanced conductivity. The subsequent chapters will address how this modification in UiO-66, with Ag_2O and PEDOT present in different locations, affects its physico-chemical and electrochemical properties.

References

[1] Safaei, M. *et al.* A review on metal-organic frameworks: Synthesis and applications. *TrAC - Trends in Analytical Chemistry* **118** 401–425, 2019.

[2] Ma, T., Li, H., Ma, J. G. & Cheng, P. Application of MOF-based materials in electrochemical sensing. *Dalton Transactions*. **49**: 17121–17129, 2020.

[3] Han, S. *et al.* Tunneling Electrical Connection to the Interior of Metal-Organic Frameworks. *J Am Chem Soc*. **137**: 8169–8175, 2015.

[4] Park, J. *et al.* Stabilization of Hexaaminobenzene in a 2D Conductive Metal-Organic Framework for High Power Sodium Storage. *J Am Chem Soc*. **140**: 10315–10323, 2018.

[5] Narayan, T. C., Miyakai, T., Seki, S. & Dincă, M. High Charge Mobility in a Tetrathiafulvalene-Based Microporous Metal–Organic Framework. *J Am Chem Soc*. **134**: 12932–12935, 2012.

[6] Sun, L., Hendon, C. H., Minier, M. A., Walsh, A. & Dincă, M. Million-Fold Electrical Conductivity Enhancement in Fe $_2$ (DEBDC) versus Mn $_2$ (DEBDC) (E = S, O). *J Am Chem Soc*. **137**: 6164–6167, 2015.

[7] Yao, M. *et al.* A Dual-Ligand Porous Coordination Polymer Chemiresistor with Modulated Conductivity and Porosity. *Angewandte Chemie International Edition*. **59**: 172–176, 2020.

[8] Kitao, T., Zhang, Y., Kitagawa, S., Wang, B. & Uemura, T. Hybridization of MOFs and polymers. *Chem Soc Rev*. **46**: 3108–3133, 2017.

[9] Goswami, S. *et al.* A porous, electrically conductive hexa-zirconium (iv/v) metal–organic framework. *Chem Sci*. **9**: 4477–4482, 2018.

[10] Atzori, C. *et al.* Effect of Benzoic Acid as a Modulator in the Structure of UiO-66: An Experimental and Computational Study. *The Journal of Physical Chemistry C*. **121**: 9312–9324, 2017.

[11] Li, X.-M. *et al.* Strategic hierarchical improvement of superprotonic conductivity in a stable metal–organic framework system. *J Mater Chem A Mater*. **7**: 25165–25171, 2019.

[12] Pham, Q.-T., Huy, B. T. & Lee, Y.-I. New highly efficient electrochemical synthesis of dispersed Ag $_2$ O particles in the vicinity of the cathode with controllable size and shape. *J Mater Chem C Mater*. **3**: 7720–7726, 2015.

[13] Haq, S. *et al.* Green Synthesis of Silver Oxide Nanostructures and Investigation of Their Synergistic Effect with Moxifloxacin Against Selected Microorganisms. *J Inorg Organomet Polym Mater*. **31**: 1134–1142, 2021.

[14] Xu, W., Dong, M., Di, L. & Zhang, X. A Facile Method for Preparing UiO-66 Encapsulated Ru Catalyst and its Application in Plasma-Assisted CO2 Methanation. *Nanomaterials*. **9**: 1432, 2019.

[15] Øien, S. *et al.* Detailed Structure Analysis of Atomic Positions and Defects in Zirconium Metal–Organic Frameworks. *Cryst Growth Des*. **14**: 5370–5372, 2014.

[16] Ag2O Crystal Structure: Datasheet from ``PAULING FILE Multinaries Edition – 2022'' in SpringerMaterials (https://materials.springer.com/isp/crystallographic/ docs/sd_0542207).

[17] Qiu, L.-G. *et al.* Facile synthesis of nanocrystals of a microporous metal–organic framework by an ultrasonic method and selective sensing of organoamines. *Chemical Communications*. **3642**, 2008.

[18] ALOthman, Z. A Review: Fundamental Aspects of Silicate Mesoporous Materials. *Materials*. **5**: 2874–2902, 2012.

[19] Brunauer, S., Emmett, P. H. & Teller, E. Adsorption of Gases in Multimolecular Layers. *J Am Chem Soc*. **60**: 309–319, 1938.

[20] Wang, T. *et al.* Functional conductive nanomaterials via polymerisation in nano-channels: PEDOT in a MOF. *Mater Horiz*. **4**: 64–71, 2017.

[21] Han, Y. *et al.* Facile synthesis of morphology and size-controlled zirconium metal–organic framework UiO-66: the role of hydrofluoric acid in crystallization. *CrystEngComm*. **17**: 6434–6440, 2015.

[22] Ahmadijokani, F. *et al.* Impact of scale, activation solvents, and aged conditions on gas adsorption properties of UiO-66. *J Environ Manage*. **274**: 111155, 2020.

[23] Bárcia, P. S. *et al.* Reverse shape selectivity in the adsorption of hexane and xylene isomers in MOF UiO-66. *Microporous and Mesoporous Materials*. **139**: 67–73, 2011.

[24] Kandiah, M. *et al.* Post-synthetic modification of the metal–organic framework compound UiO-66. *J Mater Chem*. **20**: 9848, 2010.

[25] Han, Y. *et al.* Facile synthesis of morphology and size-controlled zirconium metal–organic framework UiO-66: the role of hydrofluoric acid in crystallization. *CrystEngComm*. **17**: 6434–6440, 2015.

[26] Rutledge, S. A. & Helmy, A. S. Etch-Free Patterning of Poly(3,4-ethylenedioxythiophene)–Poly(styrenesulfonate) for Optoelectronics. *ACS Appl Mater Interfaces*. **7**: 3940–3948, 2015.

[27] Gueye, M. N., Carella, A., Faure-Vincent, J., Demadrille, R. & Simonato, J.-P. Progress in understanding structure and transport properties of PEDOT-based materials: A critical review. *Prog Mater Sci*. **108**: 100616, 2020.

[28] Du, M., Chen, X. & Zhang, K. Origins of Enhanced Thermoelectric Transport in Free-Standing PEDOT Nanowires Film Modulated with Ionic Liquid. *ACS Appl Energy Mater*. **4**: 4070–4080, 2021.

[29] Kanwat, A. & Jang, J. High work function with reduced phase separation of PSS in metal oxide modified PEDOT:PSS interlayers for organic photovoltaics. *RSC Adv*. **6**: 114800–114807, 2016.

[30] Park, J.-K. *et al.* Real-time Humidity Sensor Based on Microwave Resonator Coupled with PEDOT:PSS Conducting Polymer Film. *Sci Rep*. **8**: 439, 2018.